



Numerical and experimental analysis of the isothermal high temperature pneumoforming process

Mike Kamaliev¹ · Jan Flesch¹ · Joshua Grodotzki¹ · A. Erman Tekkaya¹

Received: 25 October 2022 / Accepted: 9 June 2023 / Published online: 4 July 2023
© The Author(s) 2023

Abstract

The isothermal high temperature pneumoforming process to form tubes at constant elevated temperatures by means of internal pressure is investigated. Two materials, a ferritic (X2CrTiNb18) and a martensitic stainless steel (X12Cr13) are used for the investigations. The required material characterization is performed at the temperature and strain rate of the actual process. A new method for quantifying thermal softening via the time-dependent decrease in static yield stress is presented. At a temperature of 1000 °C, the static yield stress decreases by 50% within 100 s for both materials. The numerical models are validated on the basis of the formed geometry and used to study the influence of maximum internal pressure, axial feed, holding time under load and die edge length on the final part geometry. It was observed, that with higher internal pressures and longer holding times smaller corner radii are formed for both materials. In contrast, a superimposed axial feed as well as the effective friction coefficient have a negligible influence on the formed geometry. With an increasing die edge length, smaller radii are formed with the ferritic stainless steel numerically and experimentally. By contrast, for the martensitic stainless steel, larger radii are observed numerically. Experimentally, the limited formability of these tubes weld seam becomes apparent. Based on the findings, process windows depending on the process parameters internal pressure and die edge length were derived. Numerically, forming limit curves of tubular semi-finished products under comparable conditions serve as a failure criterion. Good agreement with experiments was observed.

Keywords Pneumoforming · Hydroforming · Elevated temperatures · Hot stamping · Press hardening · Stainless steel

Introduction

Lightweight design is one of the key motivations for reducing CO₂ emissions. In forming technology, this objective requires processes that enable the manufacturing of components with more complex geometries and high strength at the same time. A common approach to this is forming at elevated temperatures and subsequent hardening. For sheet metal components, press hardening is already an established process [1]. In the field of internal high-pressure forming, several approaches exist to apply the advantages of hot forming (higher forming limits, lower forming forces and less springback) to closed profiles. Even though most of the processes still have a low

technology readiness level and are part of ongoing research, there are already fields of application in series production, such as the roof bows of the Ford Bronco, which are produced through form blow hardening [2].

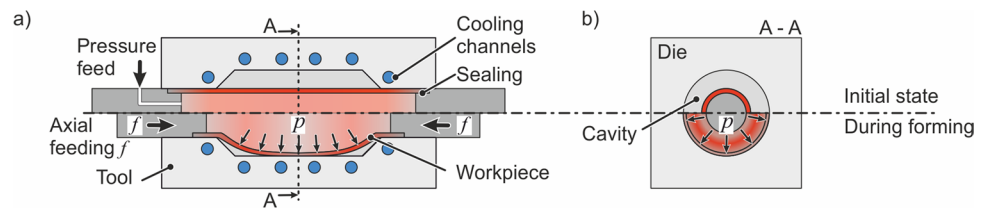
In the field of internal high pressure forming, the medium-based pressure can be used in two ways. On the one hand, actively, in which case the internal pressure is the sole agent of shaping (e.g. [3]). On the other hand passively, as a supporting internal pressure, in which case the forming is performed predominantly by a radially acting punch (e.g. [4]). In this contribution, an active internal pressure is in the focus. A general structure of such a process is shown in Fig. 1. The individual process steps are divided into heating, forming and quenching, in the same way as for press hardening.

There are several ways to heat the profiles before forming. These include heating in the furnace [5], by means of induction [6] or by resistance heating [3]. With furnaces, a homogeneous temperature distribution is achieved, but this method is associated with a transfer as well as a heat loss into the die. Induction heating has higher heating rates,

✉ Mike Kamaliev
Mike.Kamaliev@iul.tu-dortmund.de;
Office@iul.tu-dortmund.de

¹ Institute of Forming Technology and Lightweight Components, Baroper Straße 303, 44227 Dortmund, Germany

Fig. 1 Schematic of high temperature pneumoforming in the **a** front view and **b** cross-sectional view



but also requires a transfer [7] or removal of the coil [8]. Inductive heating during the forming process is not possible because the varying distance between the coil and the specimen leads to an inhomogeneous temperature distribution [9]. With resistance heating, the electrical connectors can be installed directly in the mold or on the workpiece. A transfer is thus no longer necessary [3]. On straight profiles, centrally homogeneous temperature distributions can be achieved without further measures. Temperature gradients occur in the area of the electrical connectors, the extent of which depend on the thermal parameters of the clamps and the workpiece [10]. In the case of curved specimens, a hot-spot is formed on the inner arc. This can be reduced if the current intensity is pulsed over time [11].

Gaseous media are currently preferred as forming media at hot forming temperatures. Liquid media can only be used up to approx. 300 °C. Solid media, on the other hand, typically have a low heat transfer coefficient, so that they are not suitable for processes where the active forming medium is also used as the cooling medium [12]. Commonly the gaseous medium is not pre-heated, so that it leads to a cooling of the specimen while building up the internal pressure for the forming process [13]. Simultaneously, lower forming limits are obtained and higher internal pressures are required with decreasing temperature. To prevent this cooling effect, the use of heated tools is possible, which allows for isothermal forming processes. This has already been carried out for aluminum at 500 °C. A higher degree of forming can be observed, if longer holding times at constant high temperature and pressure are used [14]. On the other hand, it is known for steel materials that an excessively high tool temperature can prevent hardening. Under non-isothermal conditions, pressures of up to 70 MPa are therefore used for steel materials [15]. If the component is to be hardened after forming, the use of suitable quenching methods is required. Similar to press hardening of sheet materials, cooled tools can be used to harden boron-manganese steels to above 500 HV5 [5]. Alternatively, the component can also be cooled with water from the inside after internal pressure forming [16].

Processes that enable isothermal forming and subsequent hardening in the die are not yet known. It is beneficial to form the profile by means of internal pressure at constant high temperatures (isothermal) so that lower pressures are required and higher forming limits are achievable. At the

same time, the potential hardening of the part after forming by means of quenching in the same machines is desired. It is apparent from the state of the art, that resistance heating is the only method that can be considered to fulfill these requirements. The tool may not heat up too much to allow cooling from the inside through the medium. In this application, compressed air is used as the forming and quenching medium. In order to meet all the stated requirements, the authors have devised a process to hot form hollow parts by means of internal pressure with the option of subsequent hardening in the tool. The experimental setup and the general feasibility of this process, called isothermal-high-temperature-pneumoforming process (IHTP-process), have already been proven in [17]. The aim of this paper is to determine the process windows for both materials and varying die edge lengths. This includes appropriate material characterization methods, the numerical modeling of the IHTP-process and an experimental validation.

Materials and methods

During hot forming, distortion of low-alloy steels occurs. Standard coatings do not allow rapid heating rates as used in the IHTP process [18]. From this point of view, suitable materials are selected and the experimental setup as well as the general process-procedure is presented. Furthermore, potentially relevant parameters for the analysis of the process are derived.

Materials

The ferritic stainless steel X2CrTiNb18 (short form for the remainder of the text and figures: *Ferrite*) and the martensitic stainless steel X12Cr13 (short form: *Martensite*) are used in the following investigations. The chemical composition of the two materials is given in Table 1. In the case of ferrite, the ductility initially reduces with increasing temperature up to approx. 700 °C before a significant improvement takes place [19]. The martensite belongs to the air hardening steels. In the as-delivered condition, it has a hardness of approx. 150 HV10. For the investigations, welded tubes with a diameter of 50 mm ($d_0 = 2 \cdot r_0$) and a wall thickness of 1 mm (s_0) are used.

Table 1 Chemical composition of the used stainless steels in wt-% without impurity [20]

	C	Cr	Ni	Ti	Nb
Ferrite (X2CrTiNb18)	0.03	17.5–18.5	-	0.1–0.6	(3·C + 0.3)·1
Martensite (X12Cr13)	0.08–0.15	11.5–13.5	0.75	-	-

Both materials exhibit increased resistance to oxidation (scale) at elevated temperatures due to their alloying constituents [21]. The formation and detachment of scale layers causes faulty temperature measurement by the optical systems and is therefore impermissible. With the thermal treatment times used for the IHTP process, this is given up to a temperature of 1000 °C.

Experimental setup and procedure

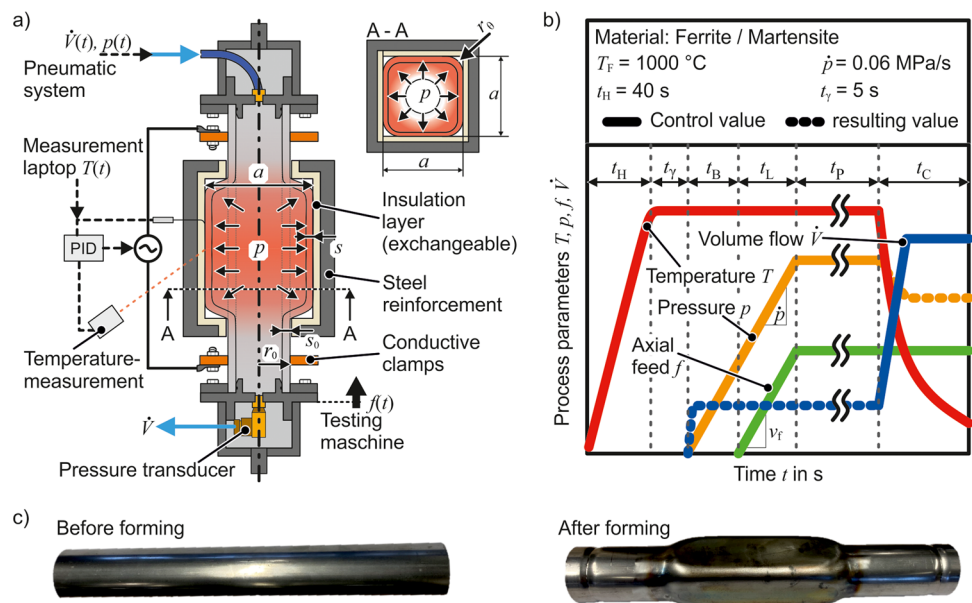
The experimental setup is shown in Fig. 2a and is identical to that of [17]. For the experiment, the tubes are sealed airtight on both sides. The media supply is connected on one side. At the other end, a valve is connected in order to be able to vary the volume flow during cooling. For heating, water cooled conductive clamps are attached to the tube with a distance of $w_0 = 190$ mm. The assembly is placed in a universal testing machine Zwick Z250 (co. ZwickRoell GmbH & Co. KG), which provides an optional axial feed. The temperature is set using a Metis M308 pyrometer and a PID controller Regulus RD (both co. Sensortherm). The pyrometer has a measuring range from 600 to 1400 °C. To measure the cooling gradients, a thermocouple is inserted in the die. The power for the resistance heating is provided by a DC-generator LAB/HP 4020 (co. ET System electronic GmbH). To define the shape, a square die with a variable edge length a is used. In addition to a steel

reinforcement, thermal and electrical insulating materials are utilized on the inside to maintain heating during forming. For this purpose, the mica paper impregnated silicone resin KS 800 M (co. AGK-Hochleistungswerkstoffe GmbH) is used. The change of the die edge length a is realized by the use of spacers and the adjustment of the insulating layer (Fig. 2a). To monitor the volumetric flow \dot{V} during forming and subsequent cooling, a VA 520 - thermal mass flow meter (co. CS-Instruments) is implemented.

The process parameters during the experiment are shown qualitatively in Fig. 2b. Initially, the profile is heated to the forming temperature $T_F = 1000$ °C within the time $t_H = 40$ s. After a dwell time of $t_\gamma = 5$ s, the pressure p is increased with a ramp of $\dot{p} = 0.06$ MPa/s. Steeper pressure ramps would lead to an undesired cooling of the sample during the inflow of the medium, which enters the forming zone at room temperature. The resulting process times can be over 100 s (depending on the maximum pressure aimed for), which is why suitability for series production in its current form is not feasible. In order to reduce the processing times, the application of more powerful generators for heating is required. These would be able to compensate the cooling effect of higher volume flows in order to maintain the isothermal process character.

After a material-specific time t_B , the bulging of the tube begins and an optional axial feed f with varying feed rates v_f can be added. First, free expansion takes place until the

Fig. 2 a Experimental setup of the isothermal high temperature pneumoforming (IHTP) process [17], b qualitative trend of the process parameters over the duration of the experiment such as c exemplary specimen out of martensitic stainless steel before and after forming



workpiece comes into contact with the die. Then there is a restricted forming of corner radii, denote with r_0 . This radius decreases as long as the forming operation continues. After the load time t_L , the maximum pressure p_{max} is reached and, if applied, the axial feed f stops for all subsequent process steps. Optionally, the internal load can be maintained for the pressure time t_p in order to further form the profile due to increasing thermal softening. Finally, the heating is stopped and the profile is quenched by a defined internal volume flow \dot{V} within a cooling time t_C . No further forming is achieved due to the accompanying drop in internal pressure and the increasing flow stresses caused by the falling temperatures. Figure 2c shows exemplary specimens from martensitic stainless steel before and after the forming process.

Parameter definition for the experimental procedure and numerical modeling

For the IHTP-process, the boundary conditions for the modelling involve the axial feed rate v_f , the pressure over time $p(t)$ and the temperature level as well as its distribution. The axial feed rate is defined as position-controlled via the universal testing machine. To validate the targeted pressure ramp, reference tests are performed prior to numeric modeling (Experimental setup and procedure section). Figure 3a shows the realized experimental setup.

Figure 3b provides the measured evolution of the process variables over time. As desired, the pressure increases with a ramp of 0.06 MPa/s. The temperature also remains almost constant during the forming process at the targeted value of 1000 °C. With the exemplary volume flow of $\dot{V} = 50$ l/min chosen here, a quenching gradient of approx. $\dot{T} = 5.87$ °C/s can be achieved. This value is calculated between forming temperature $T_F = 1000$ °C and martensite start temperature $M_S = 350$ °C. The quantitative influence of different cooling gradients is investigated in “Mechanical properties” section.

In addition to the mechanical load variables, the temperature distribution in the specimen is needed for the numeric modeling. For this purpose, a tube section is heated using the method described in “Experimental setup and procedure” section and the temperature distribution is determined with a thermographic camera thermoIMAGER TIM M1 (co. Micro-Epsilon). The camera has a limited measuring range at lower temperatures of about 600 °C. Further, deviating emission characteristics are expected with decreasing temperatures, which is why only the range with validated emission values of approx. 1000 °C are considered hereinafter. The distance of the conductive clamps is set to $w_0 = 100$ mm in order to obtain a finer resolution of the measuring range. Figure 4a shows a thermographic image of a sample heated to 1000 °C. No temperature deviations are observed over the circumference.

Fig. 3 a Actual experimental setup for the isothermal high temperature pneumoforming (IHTP) process, b measured development of the experimental parameters temperature, pressure and volume flow

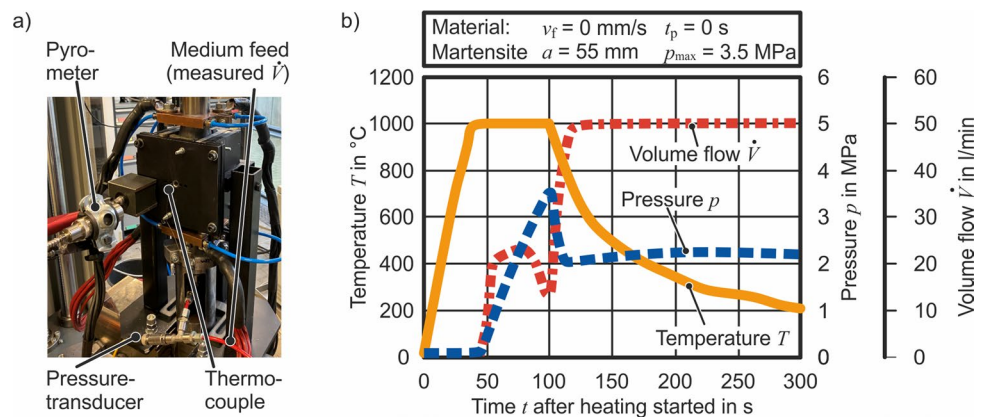
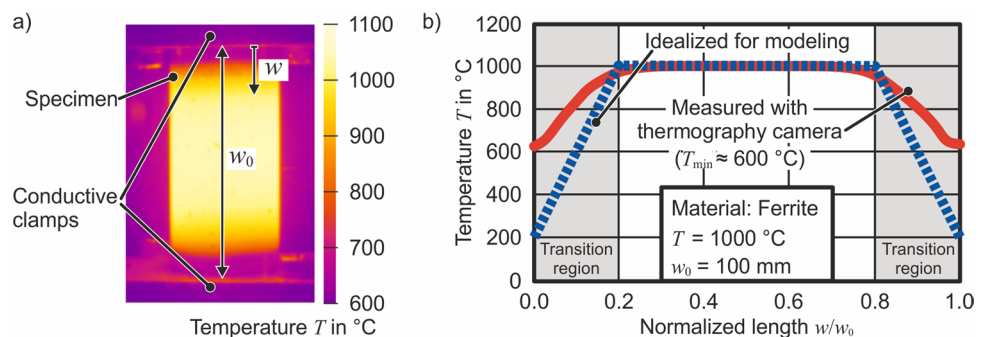


Fig. 4 a Thermographic camera image of a specimen heated to 1000 °C and b measured and idealized temperature profile along the normalized longitudinal axis of the specimen



The measured temperature gradient over the longitudinal axis can be seen in Fig. 4b. The transition area up to the target temperature of 1000 °C is approx. 20 mm per side, while the central 60 mm show a homogeneous temperature. For the numerical modeling, a linear progression is assumed for the transition region. Due to the water cooling of the conductive clamps and the limitations of the thermographic camera mentioned above, 200 °C is assumed as the lower limit.

Material characterization

To setup accurate numerical models for the IHTP-process, various key information about the material behaviour at process-relevant temperatures is required. Hence, in “Determination of elastic and plastic material properties” section hot tensile tests are performed to estimate the elastic as well as plastic behaviour. Important for this forming process is also the knowledge about the evolution of the static yield stress over time at a given constant load. Special tests were devised and the results presented in “Thermal softening behaviour under process-related conditions” section.

Table 2 Experimentally determined Young’s moduli of the two materials at specific temperatures

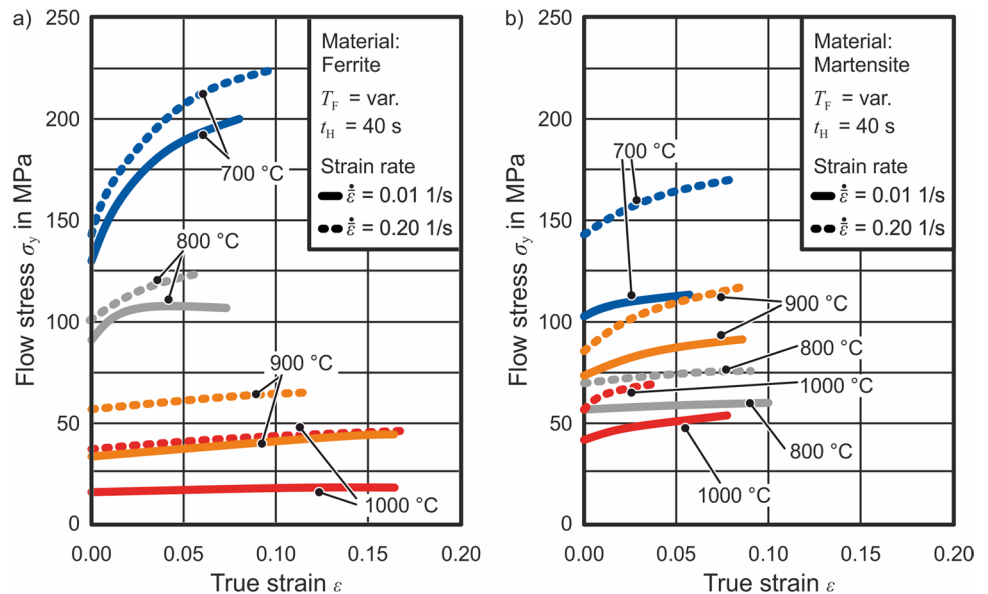
T_U [°C]	20	700	800	900	1000
Ferrite: E_F [GPa]	199.14	94.19	48.79	17.43	10.50
Martensite: E_M [GPa]	192.54	68.07	47.42	37.87	27.50

Determination of elastic and plastic material properties

Hot tensile tests are carried out to determine the thermo-mechanical properties of both materials. The heating is analogous to the isothermal high temperature pneumoforming (IHTP) process (Experimental setup and procedure section). Specimens with an initial gauge length of $l_0 = 20$ mm are tested in the Zwick Z250 universal testing machine (co. ZwickRoell GmbH & Co. KG). For the introduction of the current for resistance heating, clamping jaws made of copper are used. The elongation of the specimen is measured with a high temperature extensometer PMA-12/V7-1 (co. Maytec). The investigations will focus on the central main forming zone of the tubes (Fig. 4). Therefore, forming temperatures from $T_F = 700$ to 1000 °C, supplemented by room temperature experiments, will be investigated. The material-specific Young’s moduli for the ferritic E_F and martensitic E_M stainless steel as a function of the forming temperature T_F are summarized in Table 2. For both materials, a decrease in Young’s modulus was observed with increasing temperature. These results are in line with the state of the art (e.g. [19]).

The strain-rate and temperature-specific flow curves are partially summarized for both materials in Fig. 5. Effective strain rates of $\dot{\epsilon} = 0.01$ s⁻¹, $\dot{\epsilon} = 0.04$ s⁻¹ and $\dot{\epsilon} = 0.2$ s⁻¹ were investigated. The yield stress and strain hardening increase with decreasing forming temperature and increasing effective strain rate. An exception are the results from the martensitic stainless steel at temperatures of 800 and 900 °C. Here, due to austenitization, there is a temporary increase in the yield stress between 800 and 900 °C, before decreasing further. For ferritic stainless steel (Fig. 5a), a minimum initial yield stress of $\sigma_{y,0,F} = 17$ MPa is

Fig. 5 Experimentally determined temperature and strain rate dependent flow curves for a the ferritic- and b the martensitic stainless steel (for better clarity not all flow curves are shown)



determined. In contrast, the value for martensitic stainless steel is $\sigma_{y,0,M} = 42.5$ MPa. This deviation is representative of the different internal pressures required in the IHTP-process to achieve comparable strains. For ferritic stainless steel, almost no strain hardening is determined above 900 °C. For this reason, an extrapolation approach according to Hockett-Sherby with saturation stress is used for the later numerical investigations. For the martensitic stainless steel (Fig. 5b), an extrapolation approach according to Ludwik is chosen, since no saturation of the flow stress is determined at the most relevant forming temperature of 1000 °C. A visualization of the extrapolations and the corresponding coefficients for both materials are given in the Appendix 1.

Thermal softening behaviour under process-related conditions

In addition to the elasto-plastic characteristics, a softening effect during high temperature hydroforming is known from literature [14]: the static yield stress of a material under mechanical load decreases with increasing holding time at elevated temperatures. A comparable behaviour is known for creep of steel, where commonly higher periods (e.g. days) are investigated. To transfer this behaviour to the IHTP-process, it is necessary to determine the static yield stresses $\sigma_{S,0}$ (apparent yield stress σ_y at an effective strain rate of $\dot{\epsilon} = 0.01 \text{ s}^{-1}$) as a function of time. This time dependent values

can be considered as the lower limit for pressure-driven pneumoforming processes. To determine quantitative values for the material specific static yield stresses $\sigma_{S,0}$, tensile specimens are heated to $T_F = 1000$ °C, loaded linearly to different stress levels and held isothermally at these loads. The initial flow stress at the lowest strain rate $\sigma_{y,0}$ ($\dot{\epsilon} = 0.01 \text{ s}^{-1}$) is used as a reference for this purpose ($\sigma_{y,0,F} = 17$ MPa and $\sigma_{y,0,M} = 42.5$ MPa). Starting from these material-specific values, the mechanical load for subsequent tests is reduced in steps of 10% until no plastic deformation is detected within a holding time of $t_\sigma = 100$ s. Figure 6a shows exemplary load curves for 40, 60 and 80% of the initial flow stress $\sigma_{y,0}$ ($\dot{\epsilon} = 0.01 \text{ s}^{-1}$). The reason for this procedure is, as stated above, that for a longer time at elevated temperatures, the materials continue to soften and therefore show reduced initial yield stresses over time. To keep the influence of an effective strain rate as low as possible, all tested load levels are ramped linearly within $t_s = 30$ s (Fig. 6a). For the tested gauge length of 30 mm, this results in negligibly low effective strain rates.

The static yield stresses $\sigma_{S,0}$ as a function of the loading time t_σ are shown in Fig. 6b. For both materials, no plastic flow was detected below $0.5 \cdot \sigma_{y,0}$ ($\dot{\epsilon} = 0.01 \text{ s}^{-1}$) within $t_\sigma = 100$ s. In the range from 1.0 down to $0.5 \cdot \sigma_{y,0}$, a steady decrease of the static yield stress $\sigma_{S,0}$ is detected. As can be seen in Fig. 6b, the static yield stress decrease can be approximated by a linear relation before saturating. The mathematical relationship is explicitly given by the following equations:

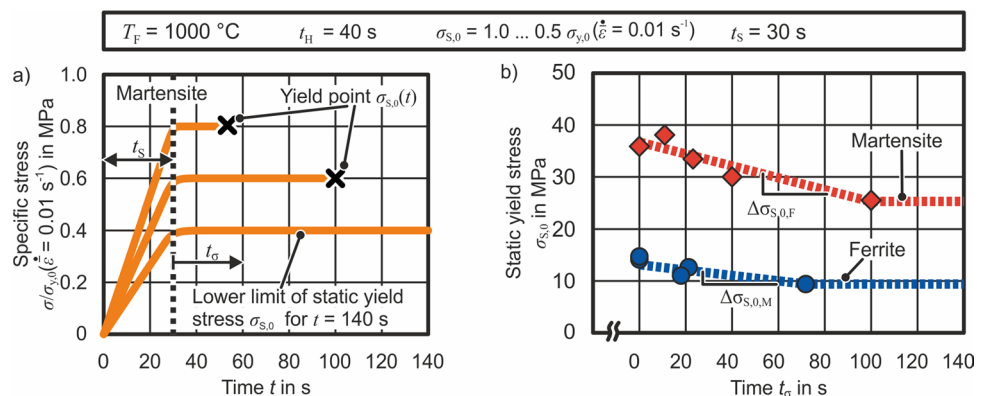
$$\text{Ferritic stainless steel : } \sigma_{S,0,F}(t_\sigma) = -0.05 \text{ MPa/s} \cdot t_\sigma + 12.9 \text{ MPa for } t_\sigma \leq 72 \text{ s} \tag{1}$$

$$\text{Martensitic stainless steel : } \sigma_{S,0,M}(t_\sigma) = -0.12 \text{ MPa/s} \cdot t_\sigma + 36.7 \text{ MPa for } t_\sigma \leq 99 \text{ s} \tag{2}$$

It can be seen that the static yield stress $\sigma_{S,0}$ of both materials is lower than the initial yield stress $\sigma_{y,0}$ at an effective strain rate of $\dot{\epsilon} = 0.01 \text{ s}^{-1}$. Also, both materials soften to about 50% of the initial yield stress $\sigma_{y,0}$ ($\dot{\epsilon} = 0.01 \text{ s}^{-1}$), with

a holding time of $t_\sigma = 72$ s for ferritic and $t_\sigma = 99$ s for martensitic stainless steel. In absolute terms, the martensitic material softens more strongly with a difference of 16.8 MPa ($42.5 \text{ MPa} - 25.7 \text{ MPa}$) than the ferritic one with 7.4 MPa

Fig. 6 Determination of static yield stresses - **a** Exemplary load curves when determining **b** the static yield stress $\sigma_{S,0}$ at different levels depending on the thermal-mechanical loading time t_σ



(17.0 MPa – 9.6 MPa). The method used here to characterize the softening of the materials does not take into account the current strain(-hardening) due to the limitations of the experimental setup. Also, the softening mechanisms at temperatures other than 1000 °C are neglected, since they are located outside the main forming zone.

Numerical investigations

To determine which process parameters have a significant influence on the IHTP-process as well as to quantify this influence for those that have, a numerical model is setup and presented in “Numerical model” section. In “Strain state and strain rate analysis of the IHTP-process” section the strain distribution and the resulting strain rate during forming are investigated, while in “Numerical analysis of the process parameter influence on the formed geometry” section the influence of the process parameters on the final geometry is evaluated. In addition, failure criteria in the form of forming limit curves (FLCs) are implemented in the simulation to show possible process limits.

Definition of the analysed process parameters

Before presenting the numerical model, the process parameters of the investigation are defined in advance. Table 3 provides an overview for the targeted study parameters. The reference processes serve as the basis for the investigations. From there, the individual parameters are varied to determine the different influences. The different maximum reference pressures for the ferrite $p_{\max,F}$ and the martensite $p_{\max,M}$ result from the different initial yield stresses from the material characterization (Fig. 6). For equipment reasons, forming pressures higher than 4 MPa cannot be used. Due to the pressure ramp controlled process design and the different strengths of the materials, the duration of the forming step is material-specific. To achieve total feeds f at a comparable level, lower feed rates v_f are used for the higher strength martensitic stainless steel. The specified

coefficients of friction were determined in advance by strip tensile tests under comparable process conditions. An investigation of the influence of the tribological conditions is planned numerically.

Numerical model

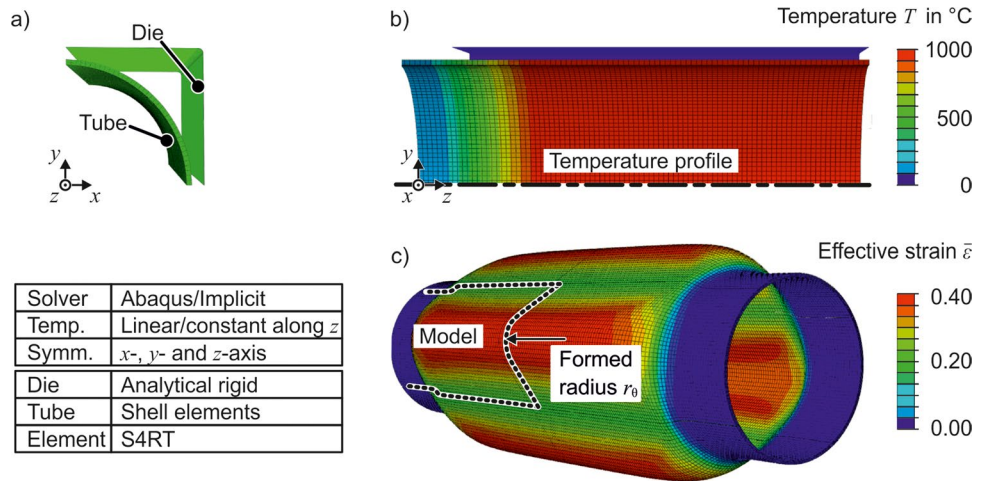
The simulation model is implemented in Abaqus/Standard and an implicit solution algorithm is used. The tube length, corresponding to the distance of the conductive clamps in the real process, is set to 190 mm and the length of the die to 150 mm. The sample is placed centrally in the die (Fig. 7a). The temperature profile is defined analogously to “Parameter definition for the experimental procedure and numerical modeling” section – first a linear transition over 20 mm and then homogeneous temperature of 1000 °C in the middle (Figs. 4 and 7b). The Young’s moduli and the flow curves from “Determination of elastic and plastic material properties” section are implemented as temperature-dependent material parameters. Depending on which holding time at maximum pressure is investigated, the corresponding static yield stress $\sigma_{S,0}$ is used for the numerical investigations (Thermal softening behaviour under process-related conditions section). The symmetry of the tube and the die in all three spatial directions is exploited whenever possible, so that only one eighth of the bodies are mapped to reduce the computation time (Fig. 7c). Exceptions are the examinations with axial feed as well as those with different failure criteria of the base metal and the weld seam.

For the modeling, the die is defined as an analytically rigid shell component and all degrees of freedom are restricted. Heat conduction to the die and wear occurring in the real process are thus neglected. Also heat conduction within the material and dissipation are not considered, given the explicitly prescribed temperature distribution. It is assumed that the deviations of the forming simulations resulting from this are justifiable. The consideration of potentially non-uniform heating due to an inhomogeneous current density distribution as well as the thermal interaction between workpiece and tool will be carried out in

Table 3 Parameter variations to be analyzed for the experimental and numeric investigations

		Maximum pressure p_{\max} [MPa]	Die edge length a [mm]	Feed rate v_f [mm/s]	Time t_p at p_{\max} [s]
Reference process	Ferrite	2.0	55	0	0
	Martensite	3.5	55	0	0
Parameter values	Ferrite	1.5 / 2.5 / 4.0	63 / 67	0.3 / 0.6	20 / 40
	Martensite	3.0 / 4.0	63 / 67	0.1 / 0.2	20 / 40
		Forming Temperature T_F [°C]	Pressure rate \dot{p} [MPa/s]	Clamp distance w_0 [mm]	Friction coefficient μ [-]
Fixed parameters	Ferrite	1000	0.06	190	0.55
	Martensite	1000	0.06	190	0.44

Fig. 7 Structure of the numerical model - **a** alignment of tube and die, **b** temperature profile of the specimen, and **c** model boundaries as well as an exemplary distribution of the effective deformation



future investigations. Since this is a thermo-mechanically coupled simulation, the element type used is S4RT, which is a thermally coupled shell element with four nodes, reduced integration and five points of integration across the thickness. The geometry is mapped via the centre contour and consists of quadratic elements with an in-plane edge length of 1 mm, which is the result of a mesh convergence analysis. The pressure rate is set to $\dot{p} = 0.06$ MPa/s, analogous to “Parameter definition for the experimental procedure and numerical modeling” section. The contact between tube and die is realized by a surface-to-surface algorithm and the friction is implemented by the Coulomb friction model. The measurement of the radii r_0 formed in the simulations is performed using a MATLAB script based on the work of Pratt [22] and basically implemented by Chernov [23].

Strain state and strain rate analysis of the IHTP-process

The numerical model is used to evaluate the strain paths as well as the final strain state. In this way, for example, critical areas can be determined for a subsequent failure analysis. Figure 8a shows the minor strain distribution of the

reference process of ferrite after forming. Figure 8b shows the strain paths of areas A to F and the final strain state of the whole component. It can be seen that with the selected process parameters, a central region forms which is subject to an almost plane strain state (see path D, E and F). Deviations from this are formed exclusively near the area which is restricted by the conductive clamps. Here, a biaxial tensile condition is observed, especially in the freely formable corner (area C). The areas D, E and F form the largest circumference in a free expansion until contact with the die in area D and show the same strain state up to that point. From then, there is only a slight increase in the tangential major strain in area D. As the process progresses, this also applies to area E. In area F, there is no contact with the die until the end of the forming. Due to the highest major strains, the areas C and F can be defined as potentially critical forming zones.

The strain rate has a pronounced effect on the flow stress of both materials (Fig. 5). To evaluate the influence on the final geometry of the components, the effective strain rates $\bar{\epsilon}$ are investigated in the areas D, E and F (Fig. 9). To separate the effects of strain rate and time dependent softening of the static yield stress, the simulation, which is presented hereafter, does not include the time dependent thermal softening

Fig. 8 **a** Numerical distribution of the minor strain in a reference process with ferritic stainless steel and **b** strain paths of selected areas as well as the final strain state of the entire component

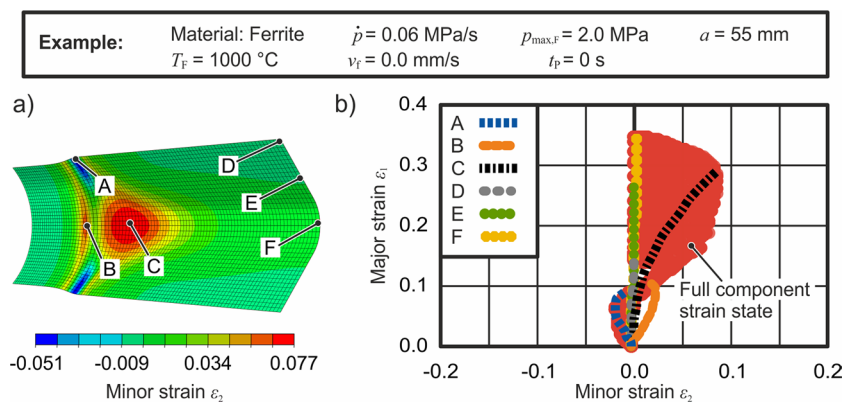
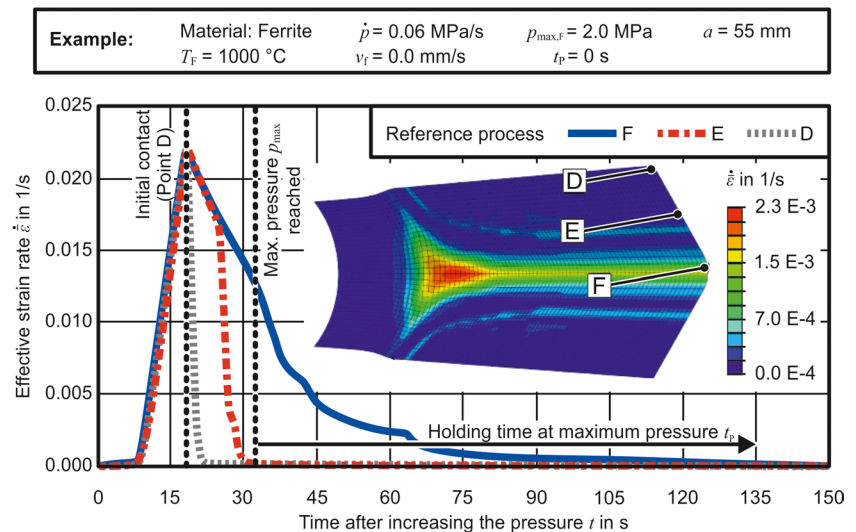


Fig. 9 Distribution of the effective strain rate in the selected areas up to and after reaching the maximum pressure p_{\max} (without reduced static yield stress $\sigma_{y,0}$)



explicitly. It can be seen that the effective strain rates initially increase at the same rate. This occurs for the duration of the free expansion until the specimen makes contact with the die. Area D is first in contact, which is why the effective strain rate $\dot{\epsilon}$ drops to zero within a short time. As the contact development progresses, the effective strain rates in the respective areas also drop to zero - as can be seen in area F. At the time when the maximum pressure p_{\max} is reached, forming only takes place in the free area (area F). Due to the continuously decreasing effective strain rate $\dot{\epsilon}$, the material softens, which allows for further forming at the same internal forming pressure. This is possible, since according to the flow behaviour at constant temperature and various strain rates, the softening for reduced strain rates is not sufficiently offset by a hardening due to increasing total strains. This observation is consistent with the state of the art [14]. The free corner forming continues until an approx. effective strain rate of $\dot{\epsilon} \approx 0 \text{ s}^{-1}$ is reached. At this stage of the forming process, the current yield stress equates the static yield stress. The internal pressure p consequently cannot provide the required stresses for further forming. In this example (Fig. 9) this particular equilibrium is reached after approx. 60 s after reaching the maximum pressure. It is expected, that by accounting for the time dependent decrease of the static yield stress $\sigma_{s,0}$ even further forming can be achieved, which will be analysed in “Numerical analysis of the process parameter influence on the formed geometry” section.

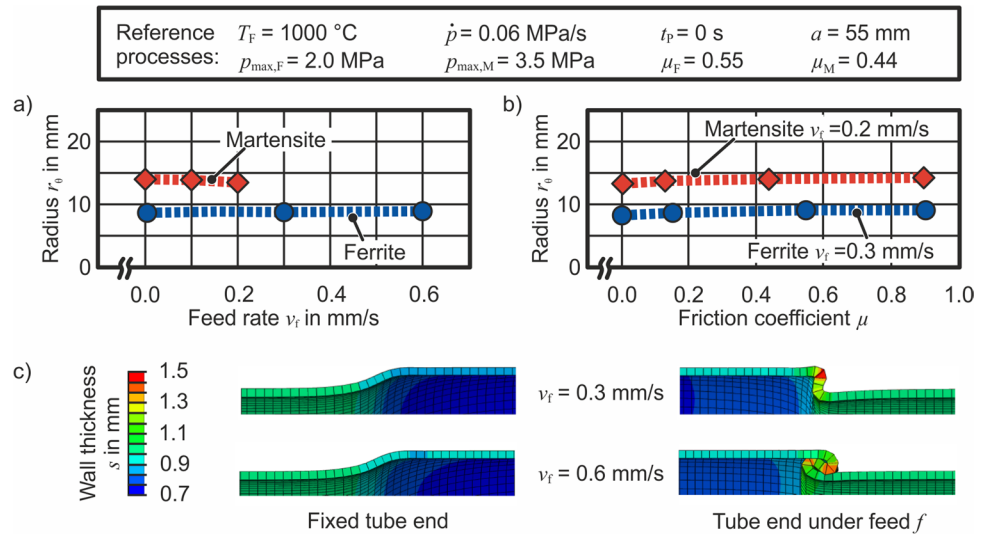
Numerical analysis of the process parameter influence on the formed geometry

In this section, the influences of the process parameters maximum pressure p_{\max} , holding time at maximum pressure t_p , axial feed rate v_f and tool edge length a on the

forming of the specimens are investigated (Table 3). The formed radii r_θ serve as a criterion for the evaluation and validation of the simulation (Fig. 7). First, the influence of the axial feed rate v_f on the formed radius r_θ is investigated. Due to the one-sided axial feed, no z-symmetry is used for these simulations. The feed rate v_f starts approximately with the expansion of the tube. Using Barlow’s formula and considering the initial yield stress $\sigma_{y,0}$ ($\dot{\epsilon} = 0.01 \text{ s}^{-1}$), this happens at pressures of $p = 0.71 \text{ MPa}$ (ferrite) and $p = 1.77 \text{ MPa}$ (martensite). This results in material-specific times of $t_B = 11.8 \text{ s}$ (ferrite) and $t_B = 29.5 \text{ s}$ (martensite) between start of the pressure ramp \dot{p} and feed rate v_f (Fig. 2b). A feed rate of $v_f = 0 \text{ mm/s}$ serves here as a reference process.

With increasing axial feed rate, no change in the formed radii is observed. The material-specific differences amount to less than 5%, so that an influence can be excluded. A potential explanation is, that the friction coefficient μ between the stainless steels to the insulating layer is too large to allow a compressive material flow in direction of the feed. For this reason, the influence of a varying friction coefficient is analyzed numerically. It can be seen that the friction coefficient also has an influence of less than 5% on the formed radius. (Fig. 10b). When comparing the tube ends (Fig. 10c), it can be seen that the region with a lower temperature is too rigid to be expanded by the internal pressure. The warmer area folds together instead of transferring the axial stresses to the central forming zone. Even with a friction coefficient of $\mu = 0$, buckling is the favoured deformation mode instead of axial compression of the homogeneous forming zone in the middle of the specimen. Not having any significant effect on the formed radii, the axial feed will no longer be taken into account for the following investigations.

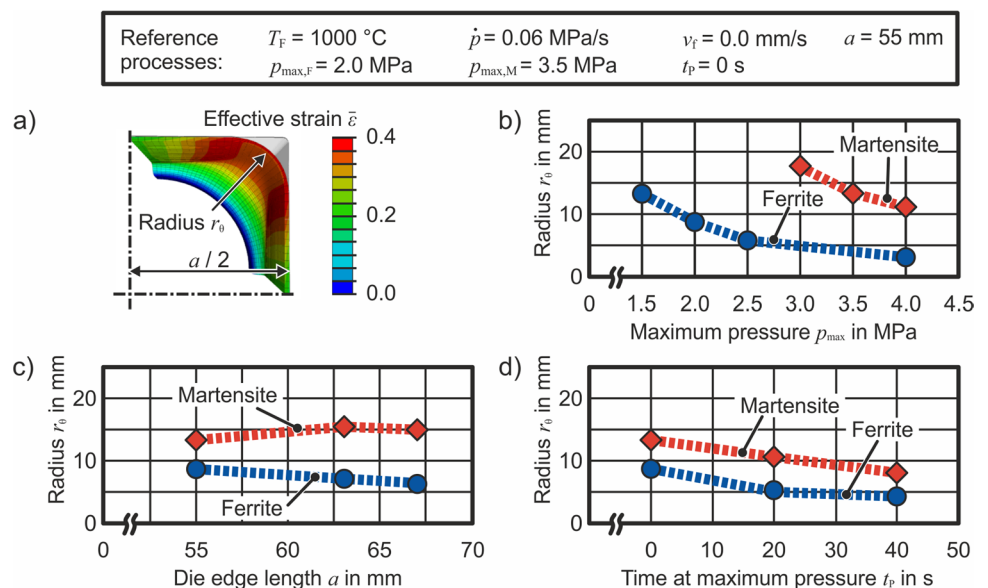
Fig. 10 Numerically determined influence of the **a** axial feed rate v_f on the formed radius r_θ , **b** the friction coefficient μ on the formed radius r_θ and **c** the geometry of both tube ends of the ferritic stainless steel at different axial feeds (reference process with $\mu_f=0.55$)



The influence of the parameters maximum pressure p_{\max} , die edge length a and holding time at maximum pressure t_p on the formed radius r_θ are summarized in Fig. 11 for both materials. With a higher maximum pressure, a smaller radius is obtained (Fig. 11b). With ferritic stainless steel, smaller radii are obtained overall due to the lower flow stresses. With increasing die edge length, smaller radii are observed for ferritic and larger radii for martensitic stainless steel (Fig. 11c). A larger die edge length results in a more pronounced free expansion before the tube comes into contact with the tool. This results in higher effective strains $\bar{\epsilon}$ with a simultaneously lower wall thickness s . When forming the corners, the area not being in contact with the die reduces with decreasing radius throughout the forming process. For the same internal pressure, smaller circumferential stresses are induced. A smaller wall thickness leads to a

higher stress in the profile at the same internal pressure. As forming progresses, the effective strain increases, resulting in strain hardening, depending on the material behaviour. All these effects have to be taken into account in order to model the material specific behaviour accurately. In ferritic stainless steel, these mechanisms are in equilibrium, with a tendency toward a predominant softening effect of decreasing wall thicknesses and the low strain hardening. For martensitic stainless steel, on the other hand, a dominant effect of strain hardening is determined, which is why the radii increase with higher die edge length. The influence of the holding time at maximum pressure t_p is shown in Fig. 11d. For the numerical analysis, the static yield stress $\sigma_{S,0}$ was calculated according to the holding time t_p using Eq. (1) or (2). With both materials, longer holding times result in smaller radii. One reason for this is the

Fig. 11 **a** Numerical model to define the formed radius r_θ as a function of **b** the maximum pressure p_{\max} , **c** the die edge length a and **d** the holding time at maximum pressure t_p (with-out failure criteria)



further forming with decreasing effective strain rate, which is accompanied by lower strength (Fig. 9). The reason for a pronounced influence in martensitic stainless steel is the higher decrease in static yield stress $\sigma_{s,0}$ (Fig. 6).

To determine whether the different parameter combinations lead to potential component cracks, failure criteria in the form of forming limit curves (FLCs) are implemented in the simulation. The material-specific FLCs are taken from studies by [24], in which the authors presented two new experimental setups to determine FLCs for the specific application in the IHTP. The resulting FLCs are shown in Fig. 12. For the details of the FLC evaluation methodology, the reader is referred to that publication. Two different forming limits are considered in hydroforming of tubes at elevated temperatures. One is the limit of free expansion (without tool contact) and a second is the limit of contact-bound forming (restricted - with partial tool contact). The ferrite's (Fig. 12a) limit of free expansion is established by a tangential instability, while the martensite's (Fig. 12b) limit is defined by a crack of the weld seam. In the numerical investigations with the martensitic stainless steel, two separate failure criteria are consequently used for the base metal and the weld seam (z-symmetry only). In contrast, the restricted FLCs represent the maximum strains of the base material, e.g. when forming the radii during the IHTP-process.

In order to predict the influence of the different parameters on the final strain distribution and the potential risk before failure, the maximum values of the relevant process parameters (Fig. 12), leading to highest major strains for both materials, are analyzed numerically. In addition to the references, these include simulations with the maximum pressures $p_{\max} = 4.0$ MPa, the largest die edge length $a = 67$ mm and the longest holding time at maximum pressure $t_p = 40$ s. Depending on the die edge length a , the free expansion results in a major strain of about $\epsilon_1(a = 55 \text{ mm}) = 0.1$, $\epsilon_1(a = 63 \text{ mm}) = 0.23$ and $\epsilon_1(a = 67 \text{ mm}) = 0.29$, at the moment of the first contact with the die. From the numeric it is known, that from this point only a slight increase of the

major strain is formed in the area first in contact (not separately shown in Fig. 12). The FLCs for free expansion should not be exceeded in this region (area D - Fig. 8).

For the ferritic stainless steel (Fig. 12a), the limit of free expansion is not exceeded at any parameter combination. At maximum pressure or maximum holding time, no failure is determined numerically. With a die edge length of $a = 67$ mm, also no failure is observed, but critical areas are close to the FLC. In the case of the martensitic stainless steel (Fig. 12b), the final strain states are less pronounced due to the higher strain hardening. There is no risk of base material failure with any parameter set. In return, the risk of weld seam failure already exists, when a total free expansion process of more than 63 mm is included.

Experimental investigations

To validate the simulation, experiments with identical parameters are performed. The formed corner radius r_0 serves as a comparative value. The results from simulation and experiment are compared and the deviations are determined. The validated simulation is used to establish exemplary process windows for the respective materials and semi-finished products.

Validation of the numerical model

For the validation of the numerical results, IHTP-experiments are performed according to Fig. 2, using the parameters of Table 3. The formed radii r_0 as a function of the parameters maximum pressure p_{\max} , die edge length a and holding time at maximum pressure t_p are shown in Fig. 13, including the numerical results. The radii were measured centrally (Fig. 13a) on the specimen with a VR5200 profilometer (co. Keyence).

The influence of the maximum pressure p_{\max} (Fig. 13b) shows a qualitatively comparable trend for both materials to the numerical investigations. With increasing maximum

Fig. 12 Forming limit curves [24] as well as final strain states at upper bounds of various parameters for **a** the ferritic and **b** the martensitic stainless steel

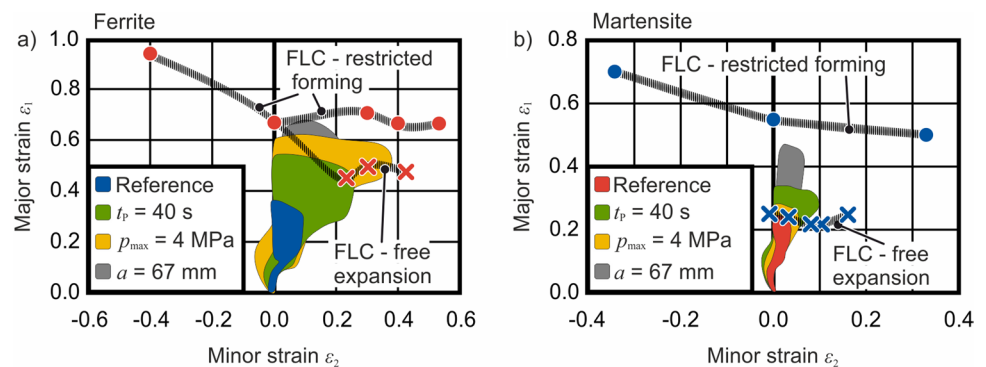
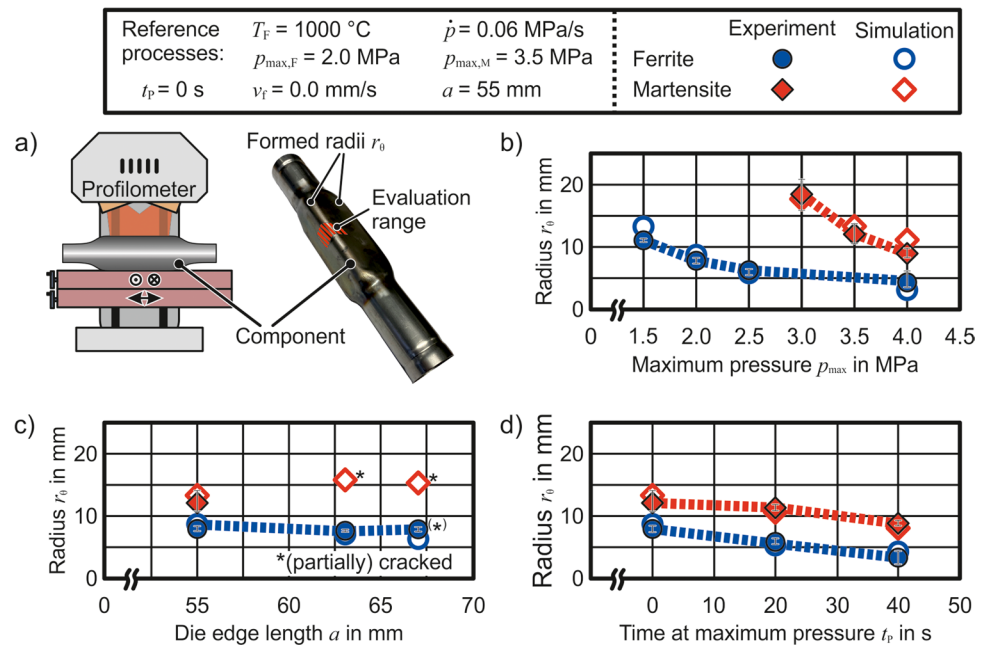


Fig. 13 Experimental and numerical (with failure criteria) correlation between formed radii r_θ and selected process parameters - **a** range of evaluation (experiment), **b** influence of maximum pressure p_{\max} , **c** influence of tool edge length a as well as **d** influence of holding time at maximum pressure t_p



pressure ($p_{\max,F}$ for ferrite and $p_{\max,M}$ for martensite), smaller radii r_θ are formed. A regressive relationship can be seen for both materials. It can be assumed that the formed radius is subject to saturation with increasing load, which cannot be achieved in these investigations due to the pressure limitation of 4 MPa. With a variation of the die edge length a , the experimental results show qualitatively the same trend as the numeric investigations (Fig. 13c). For the ferritic stainless steel, partial failure of the specimens occurred at $a = 67$ mm. With increasing die edge length, only a small change in the formed radius is determined. In the case of martensitic stainless steel, the specimens fail when the die edge length is increased to $a = 63$ mm or more. Experimental radii could therefore not be determined. With an increasing hold time at maximum pressure t_p , decreasing radii are detected experimentally, as predicted numerically. This is caused by thermal softening and the possible decrease in strain rate over time (see sections [Thermal softening behaviour under process-related conditions](#) and [Numerical analysis of the process parameter influence on the formed geometry](#)).

In some cases (e.g. for ferrite in Fig. 13d for $t_p = 40$ s) the absolute values of both experiments and simulations are small. Using those as a basis for percentual comparison would result in a poor predictive performance of the simulations, even though the associated accuracy can be considered high. Therefore, the percentual deviation between experiment and simulation is calculated with both referring to the initial tube radius r_0 . The mathematical expression for this relative deviation δ_{Rel} is given by the following relation:

$$\delta_{\text{Rel}} = \left| \frac{(r_0 - r_{\theta,\text{Num}}) - (r_0 - r_{\theta,\text{Exp}})}{(r_0 - r_{\theta,\text{Exp}})} \right| \cdot 100\% \quad (3)$$

When comparing the numerical and experimental results, average deviations of less than 10% are obtained (Table 4). The numerical setup can therefore be considered validated. In some cases, above-average deviations are found. This concerns investigations with a maximum pressure p_{\max} of 15 bar for ferritic as well as 35 and 40 bar for martensitic stainless steel. The cause for these higher than average deviations between simulations and experiments is assumed to be related to the applied material model. Due to the limited strains in the tensile test and the high effective strains that are achieved in the IHTP-process, there is an uncertainty in the extrapolated flow curves used in the simulations.

Mechanical properties

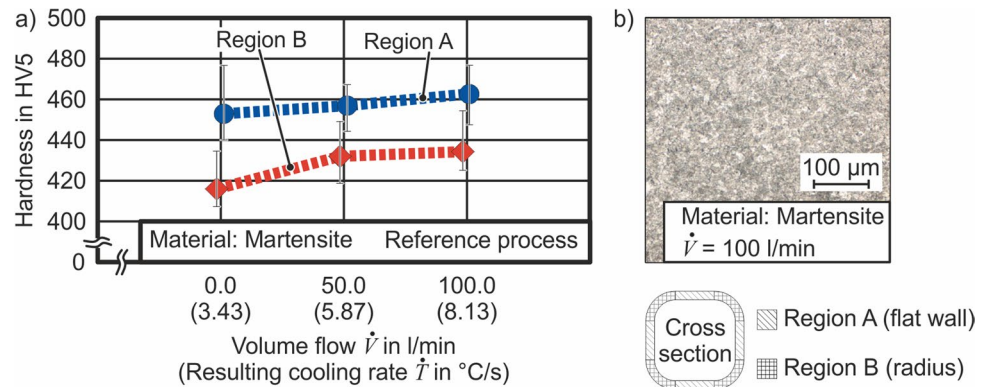
The determination of the mechanical parameters in hardness measurements as a function of the volume flow \dot{V} or the resulting cooling rate \dot{T} was carried out in previous research and published in [17]. The ferritic stainless steel cannot be hardened and was therefore not used for these investigations. The measurements in this section were carried out consequently only on the martensitic stainless steel. In the as-delivered condition, the material has a hardness of approx. 150 HV5. Figure 14a shows the hardness measurements in HV5 as a function of the volume flow \dot{V} used for quenching. The highest determined quenching gradients of $\dot{T} = 8.13\text{ °C/s}$ were obtained with a flow rate of $\dot{V} = 100\text{ l/min}$.

Table 4 Comparison of experimental and numerically determined radii r_θ as well as the parameter-specific deviation δ_{Rel}

	Corner Radii r_θ Ferritic stainless steel			Corner Radii r_θ Martensitic stainless steel		
	Experiment $r_{\theta,Exp}$ [mm]	Simulation $r_{\theta,Num}$ [mm]	Deviation δ_{Rel} [%]	Experiment $r_{\theta,Exp}$ [mm]	Simulation $r_{\theta,Num}$ [mm]	Deviation δ_{Rel} [%]
$p_{max} = 1.5$ MPa	11.28	13.43	15.6	-	-	-
$p_{max} = 2.0$ MPa	8.00	8.79	4.63	-	-	-
$p_{max} = 2.5$ MPa	6.19	5.95	1.29	-	-	-
$p_{max} = 3.0$ MPa	-	-	-	18.47	18.29	2.78
$p_{max} = 3.5$ MPa	-	-	-	12.17	14.15	15.44
$p_{max} = 4.0$ MPa	4.79	3.18	7.97	9.02	11.59	16.08
$a = 63$ mm	7.70	7.64	0.32	crack	crack	-
$a = 67$ mm	7.87	6.79	6.32*	crack	crack	-
$t_p = 20$ s	5.7	5.48	1.15	11.36	10.37	7.25
$t_p = 40$ s	3.76	4.89	5.32	8.94	8.79	0.92
Average			5.32			8.49

*Partially cracked

Fig. 14 a Determined hardness HV5 depending on the volume flow \dot{V} used for cooling or the resulting cooling rate \dot{T} and **b** Exemplary microstructure after quenching (Region A) – etched with Adler [17]



Such cooling conditions are not sufficient to harden boron-manganese steels, for example 22MnB5. For the martensitic stainless steel used in this contribution, which is considered to be an air hardening steel, the cooling conditions are sufficient. It can be seen that, that the components are hardened by the quenching gradients \dot{T} achieved. On average, at least 400 HV5 were measured. In micrographs (Fig. 14b), a martensitic microstructure was found throughout. The values in the flat wall are higher than those in the radius. Due to the air-hardening properties of the martensitic stainless steel, it is assumed that the measured hardness difference cannot be attributed to a different cooling rate alone (e.g. due to inhomogeneous volume flows). At this point, two potential hypotheses based on material mechanisms are proposed. On the one hand, the higher shape changes in the radii can cause a shift in the phase transformation points, so that

other phases besides martensite are formed. This material behavior is known, for example, from the press hardening of boron-manganese steels [25]. On the other hand, it is possible that a different temporal temperature profile is present in the radii during the forming process. In the case of martensitic stainless steels, this can influence carbide dissolution. For example, if lower temperatures are present, fewer carbides will dissolve. As a result, a greater proportion of carbon is bound during the martensitic transformation, resulting in a decrease in hardness [26]. At this point, however, these are only hypotheses, which will be investigated in future work.

Process windows

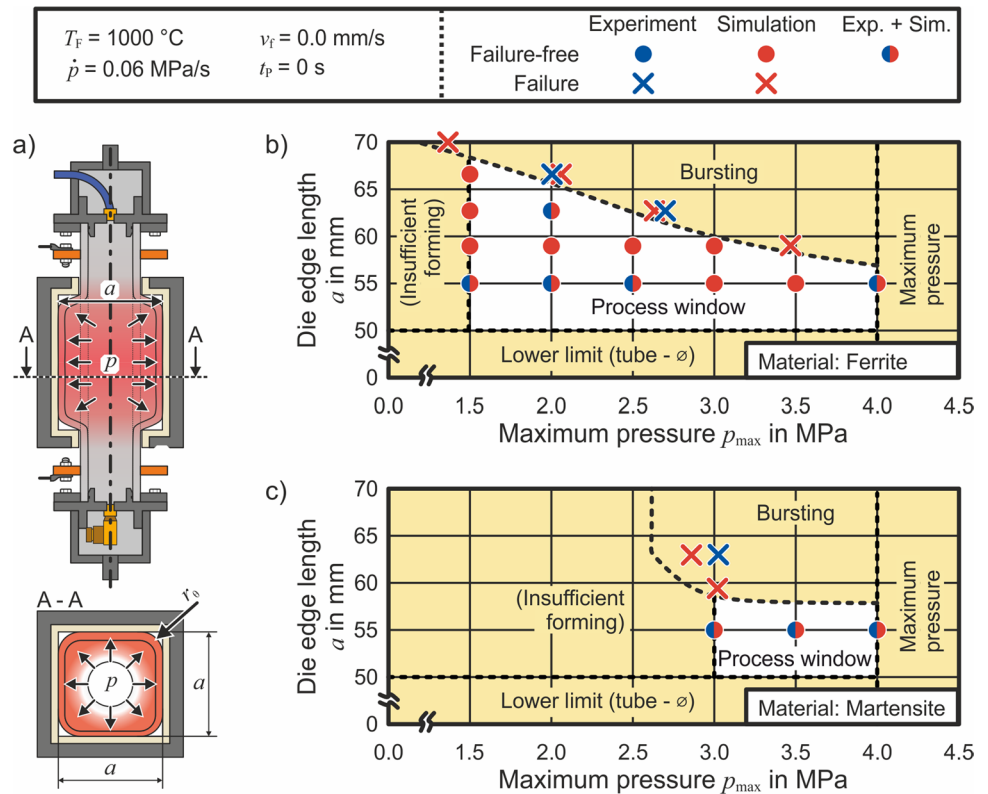
Several approaches are possible when setting up process windows. In this article, for example, one process

window is to be set up for each material, which takes into account the relationship between the die edge length a and the maximum internal pressure p_{max} . Conversely, the feed rate v_f and the holding time at maximum pressure t_p are not taken into account. Experimental as well as numerical data are used for this purpose. To determine the experimental process limits, tests are conducted with die edge lengths of $a = 55$ mm; 63 mm such as 67 mm and increasing internal pressure p_{max} until specimen failure occurs, in addition to those already carried out. For the numerical limits, die edge lengths of $a = 59$ and 70 mm are added. Figure 15 shows the geometric boundary conditions (Fig. 15a) and the process windows setup. The used initial tube diameter of 50 mm serves as the lower limit. For smaller die edge lengths, a separate die with movable tool components would be required. The upper limit results from the failure due to cracking of the specimens. The maximum available pressure of the system of $p_{max} = 4$ MPa serves as the upper pressure limit. The left limit is defined by insufficient shaping. Since this is based on a subjective assessment, it is not considered further and is only shown for illustrative purposes.

For the ferritic stainless steel (Fig. 15b), no failure was observed with die edge lengths of $a = 55$ mm. When

increasing the geometry to $a = 59$ mm, a failure of the specimen at $p_{max,Num} = 34.6$ bar is numerically is predicted. At $a = 63$ mm, the specimen failed at $p_{max,Exp} = 26.8$ bar (experiment) and $p_{max,Num} = 26.3$ bar. With $a = 67$ mm, on the other hand, the values are $p_{max,Exp} = 20.0$ bar and $p_{max,Num} = 20.6$ bar. With a die edge length of $a = 70$ mm, the specimen fails at a pressure of $p_{max,Num} = 13.1$ bar. In the case of martensitic stainless steel (Fig. 15c), a smaller process window is obtained. The reasons for this are, on the one hand, the higher pressures required for forming the radii. On the other hand, the weld seam is a weak point during free expansion, which at the same time limits the die edge length upwards. No failure is observed for a die edge length of $a = 55$ mm. With $a = 59$ mm, a failure of the weld is numerically detected at a pressure of $p_{max,Num} = 30.1$ bar. At $a = 63$ mm, the specimen failed at $p_{max,Exp} = 30.3$ bar and $p_{max,Num} = 28.1$ bar. Larger die edge lengths are no longer investigated, since failure already occurs before tool contact. The deviations between the experimental and numerical failure pressure are at maximum 3.0% for the ferritic and 7.3% for the martensitic stainless steel, therefore the numerical results with failure criteria results are all considered validated.

Fig. 15 Process window for the isothermal high temperature pneumoforming (IHTP) process – **a** Geometries of the process as well as established process windows for **b** the ferritic and **c** the martensitic stainless steel



Conclusion

The isothermal high temperature pneumoforming (IHTP) process was investigated experimentally and numerically. In this process, the temperature (here: 1000 °C) is kept constant in order to form square profiles from ferritic (X2CrTiNb18) and martensitic (X12Cr13) stainless steel tubes by means of internal pressure. Subsequently, the martensitic components can optionally be quenched and hardened by a volume flow of the gaseous forming media from the inside. The influences of the process parameters axial feed rate v_f , maximum internal pressure p_{\max} , tool edge length a and holding time at maximum pressure t_p on the final geometry were investigated. Suitable material characterization methods were developed and carried out in order to provide the required parameters for the numerical investigations. For the IHTP-process, taking into account the parameters mentioned above, the following findings are derived:

- With a higher maximum internal pressure p_{\max} , smaller shaped radii r_θ are achieved with both materials numerically and experimentally. The reachable degree of deformation is essentially dependent on the flow stress of the material.
- With longer holding times at maximum pressure t_p , smaller radii r_θ are formed with both materials numerically and experimentally. This is due to the continuous decrease of the strain rate, which leads to a lower flow stress σ_y . Simultaneously, a continuous decrease of the static yield stress $\sigma_{s,0}$ is observed at temperatures of 1000 °C with increasing holding time t_p . This softening can be determined by isothermal mechanical loading at different levels, taking the holding time into account. For both materials, the static yield stresses decrease by up to 50% within 100 s.
- With an increasing die edge length a (square die), smaller radii are formed in the ferritic stainless steel numerically

and experimentally. In the case of the martensite, larger radii are achieved numerically (in the experiment, only one die edge length a resulted in failure-free components). Several mechanisms act simultaneously. Some promote the forming (e.g. decreasing wall thickness), others impair it (e.g. work hardening). The ferritic stainless steel exhibits lower work hardening, which is why the beneficial mechanisms are predominant. For the martensitic stainless steel, the opposite is the case due to the higher work hardening.

- Using temperature distributions such as those determined here, the axial feed rate v_f has no influence on the formed radii r_θ , regardless of the material used. This is the result of both simulations and experiments. It was found numerically that even with a friction coefficient of $\mu=0$, axial buckling occurs instead of compression of the central forming zone.
- The determined forming limit curves (FLCs) from [24] are used as failure criteria. When setting up process windows, taking into account the die edge length a as well as the maximum internal pressure p_{\max} , the deviations of numerical and experimental failure parameters are at maximum 3.0% (ferrite) and 7.3% (martensite). The FLCs are considered suitable to model the failure criteria in the IHTP-process, so that it would be possible to set up process windows for any geometry.

When comparing the decrease in radius during forming between numerical simulations and experiment, average deviations of 5.32% (ferrite) and 8.49% (martensite) are obtained, hence rendering the simulations as validated. Slight deficiencies are found in the material characterization. On the one hand, experiments are needed that allow characterization up to higher effective strains under near-process conditions. Thus, the uncertainty by extrapolation can be reduced. A potential approach would be the hot-tube-bulge test [24]. Furthermore, a strain-based characterization of the thermal softening would be useful. Again, limitations of the hot tensile test are a hindrance.

Appendix 1: Extrapolation coefficients

In the following, the used approaches and coefficients for the flow curve extrapolation of the ferritic (Table 5) and martensitic (Table 6) stainless steel are presented.

Table 5 Hockett-Sherby extrapolation coefficients for the ferritic stainless steel

Material	T_F in °C	$\dot{\epsilon}$ in 1/s	Hockett-Sherby extrapolation coefficients				
			σ_{HS}	$\sigma_{y,HS}$	m	n	
Ferritic stainless steel	20	0.01	578.18	313.00	14.16	1.09	
		700	0.01	214.33	124.40	15.98	0.79
			0.04	251.45	150.91	12.15	0.87
			0.2	234.21	162.50	24.36	1.06
	800	0.01	113.85	96.61	274.08	1.11	
			0.04	153.60	93.37	18.63	0.98
			0.2	144.33	119.93	72.20	1.21
	900	0.01	43.14	36.20	35.20	1.18	
			0.04	64.25	57.76	219.43	1.92
			0.2	92.81	65.24	1.88	0.78
	1000	0.01	19.64	16.98	19.69	1.50	
			0.04	35.73	31.53	10.10	1.06
		0.2	46.86	36.72	7.71	0.94	

$$\sigma_y(\epsilon) = \sigma_{HS} - (\sigma_{HS} - \sigma_{y,HS}) \cdot e^{-m \cdot \epsilon^n}$$

Table 6 Ludwik extrapolation coefficients for the martensitic stainless steel

Material	T_F in °C	$\dot{\epsilon}$ in 1/s	Ludwik extrapolation coefficients			
			$\sigma_{L,0}$	C	n	
Martensitic stainless steel	20	0.01	301.00	1211.54	0.51	
		700	0.01	102.71	42.05	0.49
			0.04	118.30	85.92	0.55
			0.2	143.72	150.61	0.66
	800	0.01	56.11	40.26	0.91	
			0.04	69.41	29.64	0.62
			0.2	85.26	51.42	0.66
	900	0.01	72.92	86.08	0.60	
			0.04	84.80	130.05	0.56
			0.2	108.91	170.98	0.58
	1000	0.01	42.54	46.81	0.57	
			0.04	56.60	68.40	0.51
		0.2	75.55	103.12	0.56	

$$\sigma_y(\epsilon) = \sigma_{L,0} + C \cdot \epsilon^n$$

The flow curves resulting from hot tensile tests with varying temperature such as strain rate including the corresponding extrapolations are shown in Fig. 16 (ferrite) and Fig. 17 (martensite)

Fig. 16 Flow curves and extrapolations for the ferritic stainless steel (for better clarity not all flow curves are shown)

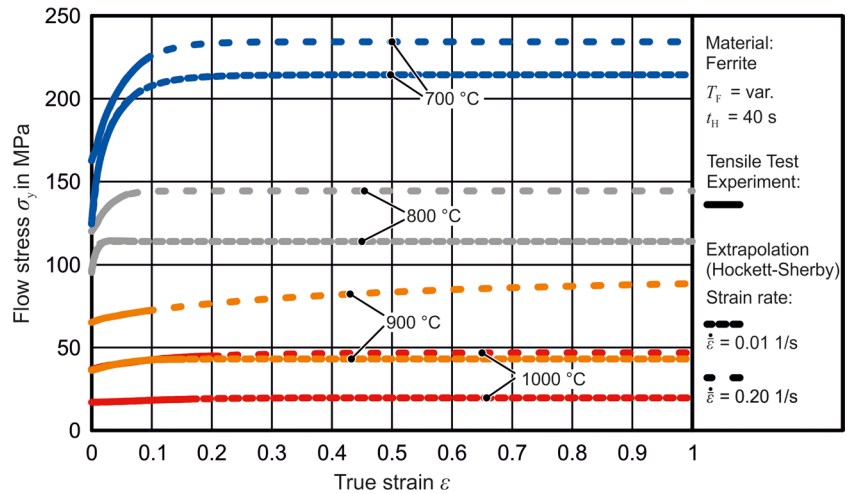
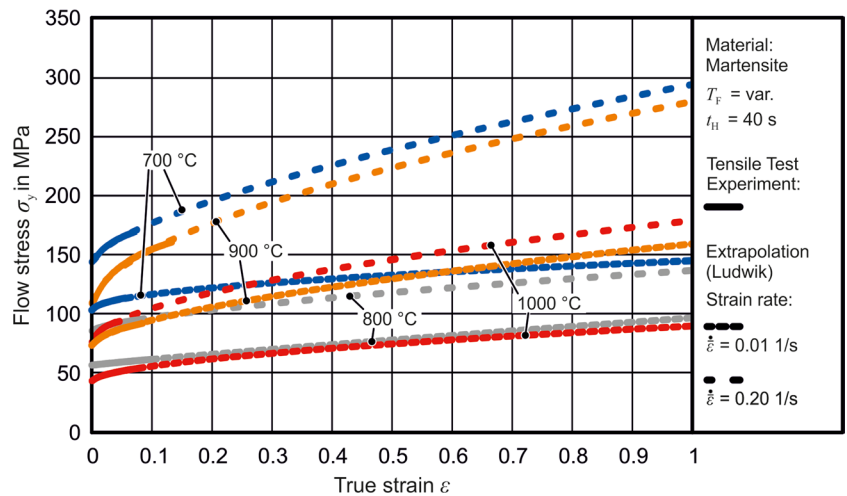


Fig. 17 Flow curves and extrapolations for the martensitic stainless steel (for better clarity not all flow curves are shown)



Authors' contributions Conceptualization: Kamaliev M and Flesch J; Methodology: Kamaliev M and Flesch J; Validation: Flesch J; Formal analysis: Kamaliev M and Grodotzki J; Investigation (experimental/analytical/numerical): Kamaliev M and Flesch J; Writing—original draft preparation: Kamaliev M and Flesch J; Writing—review and editing: Grodotzki J and Tekkaya AE; Visualization: Kamaliev M; Supervision: Grodotzki J and Tekkaya AE; Project administration: Tekkaya AE; Funding acquisition: Tekkaya AE.

Funding Open Access funding enabled and organized by Projekt DEAL. This Project is supported by the Federal Ministry for Economic Affairs and Climate Action (BMWK) on the basis of a decision by the German Bundestag (project number: ZF4101119US9). Its financial support is greatly acknowledged.

Declarations

Conflict of interest The authors declare that they have no conflict of interest.

Open Access This article is licensed under a Creative Commons Attribution 4.0 International License, which permits use, sharing, adaptation, distribution and reproduction in any medium or format, as long as you give appropriate credit to the original author(s) and the source, provide a link to the Creative Commons licence, and indicate if changes were made. The images or other third party material in this article are included in the article's Creative Commons licence, unless indicated otherwise in a credit line to the material. If material is not included in the article's Creative Commons licence and your intended use is not permitted by statutory regulation or exceeds the permitted use, you will need to obtain permission directly from the copyright holder. To view a copy of this licence, visit <http://creativecommons.org/licenses/by/4.0/>.

References

1. Karbasian H, Tekkaya AE (2010) A review on hot stamping. *J Mater Process Technol* 210(15):2103–2118

2. Sullivan M, Jones R, Conrod B et al (2022) Tailor welded tube for form blow hardened body structure enabling weight efficient open-air top. 8th Int Conf Hot Sheet Metal Form High-Performance Steel 8:453–460
3. Maeno T, Mori K-i, Unou C (2014) Improvement of die filling by prevention of temperature drop in gas forming of aluminium alloy tube using air filled into sealed tube and resistance heating. *Procedia Eng* 81(2):2237–2242
4. Maeno T, Mori K, Adachi K (2014) Gas forming of ultra-high strength steel hollow part using air filled into sealed tube and resistance heating. *J Mater Process Technol* 214(1):97–105
5. Paul A, Reuther F, Neumann S et al (2017) Process simulation and experimental validation of hot metal gas forming with new press hardening steels. *J Phys Conf Ser* 896:12051
6. Wu X, Liu Y, Zhu F et al (2001) Elevated temperature formability of some engineering metals for gas forming of automotive structures. *SAE Transactions* 110(5):1045–1056
7. Neugebauer R, Schieck F, Werner M (2011) Tube press hardening for lightweight design. ASME 2011 International Manufacturing Science and Engineering Conference, Corvallis, USA, 1:495–502
8. Yi HK, Pavlina EJ, van Tyne CJ, Yi HK, Pavlina EJ, Van Tyne CJ, Moon YH (2008) Application of a combined heating system for the warm hydroforming of lightweight alloy tubes. *J Mater Process Technol* 203(1-3):532–536
9. Elsenheimer D, Groche P (2009) Determination of material properties for hot hydroforming. *Prod Eng Res Devel* 3(2):165–174
10. Maeno T, Mori K-i, Fujimoto K (2014) Hot gas bulging of sealed aluminium alloy tube using resistance heating. *Manuf Rev* 1:5
11. Bach M, Degenkolb L, Reuther F et al (2020) Conductive heating during press hardening by hot metal gas forming for curved complex part geometries. *Metals* 10(8):1104
12. Chen H, Güner A, Khalifa NB et al (2016) Granular media-based tube press hardening. *J Mater Process Technol* 228(4):145–159
13. Drossel W-G, Pierschel N, Paul A, Drossel W-G, Pierschel N, Paul A, Katzfuß K, Demuth R (2014) Determination of the active medium temperature in media based press hardening processes. *J Manuf Sci Eng* 136(2):21013
14. Nasrollahzade M, Jalal Hashemi S, Moslemi Naeini H et al (2020) Investigation of hot metal gas forming process of square parts. *J Comput Appl Res Mech Eng* 10(1):125–138
15. Paul A, Strano M (2016) The influence of process variables on the gas forming and press hardening of steel tubes. *J Mater Process Technol* 228:160–169
16. Lanzerath H, Tuerk M (2015) Lightweight potential of ultra high strength steel tubular body structures. *SAE International. J Mater Manuf* 8(3):813–822
17. Kamaliev M, Kolpak F, Tekkaya AE (2022) Isothermal high temperature pneumoforming of stainless steel tubes at low pressure levels. In: Oldenburg M, Hardell J, Casellas D (eds), 8th International conference on hot sheet metal forming of high-performance steel, vol 8. Barcelona, pp 615–622
18. Kolleck R, Veit R (2010) Inductive heating of Al/Si-coated boron alloyed steels. In: Kolleck R (ed) 28th International deep drawing research group conference. Graz
19. Manninen T, Säynäjäkangas J (2012) Mechanical properties of ferritic stainless steels at elevated temperature. *Stainless Steel in Structures - Fourth International Experts Seminar*, Ascot
20. DIN EN 10088-1 (2014) Nichtrostende Stähle – Teil 1: Verzeichnis der nichtrostenden Stähle. Beuth Verlag, Berlin
21. Wood GC (1962) The oxidation of iron-chromium alloys and stainless steels at high temperatures. *Corros Sci* 2(3):173–196
22. Pratt V (1987) Direct least-squares fitting of algebraic surfaces. *ACM SIGGRAPH Computer Graphics* 21(4):145–152
23. Chernov N (2022) Circle Fit (Pratt method). <https://www.mathworks.com/matlabcentral/fileexchange/22643-circle-fit-pratt-method>. Accessed 06 Jul 2022
24. Kamaliev M, Kolpak F, Tekkaya AE (2022) Isothermal hot tube material characterization – forming limits and flow curves of stainless steel tubes at elevated temperatures. *J Mater Process Technol* 309:117757
25. Helmholz R, Sunderkoetter C, Plath A et al (2015) Optimization of finite element simulation for press hardening processes. In: Steinhoff K, Oldenburg M, Prakash B (eds) 5th International conference on hot sheet metal forming of high performance steel, vol 5. Toronto, pp 801–809
26. Barlow LD, Du Toit M (2012) Effect of austenitizing heat treatment on the microstructure and hardness of Marten-sitic stainless steel AISI 420. *J Mater Eng Perform* 21(7):1327–1336

Publisher's note Springer Nature remains neutral with regard to jurisdictional claims in published maps and institutional affiliations.